Journal of Computational Physics 348 (2017) 259–270

Contents lists available at ScienceDirect

Journal of Computational Physics

www.elsevier.com/locate/jcp

MUSIC algorithm for location searching of dielectric anomalies from *S*-parameters using microwave imaging

Won-Kwang Park [a,*], Hwa Pyung Kim [b], Kwang-Jae Lee [c], Seong-Ho Son [c,**]

[a] *Department of Information Security, Cryptology, and Mathematics, Kookmin University, Seoul, 02707, Republic of Korea*
[b] *Department of Computational Science and Engineering, Yonsei University, Seoul, 03722, Republic of Korea*
[c] *Radio Environment & Monitoring Research Group, Electronics and Telecommunications Research Institute, Daejeon, 34129, Republic of Korea*

ARTICLE INFO

Article history:
Received 25 April 2017
Received in revised form 5 July 2017
Accepted 17 July 2017
Available online 24 July 2017

Keywords:
MUltiple SIgnal Classification (MUSIC)
Microwave imaging
S-parameters
Multi-Static Response (MSR) matrix
Bessel function
Experimental results

ABSTRACT

Motivated by the biomedical engineering used in early-stage breast cancer detection, we investigated the use of MUltiple SIgnal Classification (MUSIC) algorithm for location searching of small anomalies using *S*-parameters. We considered the application of MUSIC to functional imaging where a small number of dipole antennas are used. Our approach is based on the application of Born approximation or physical factorization. We analyzed cases in which the anomaly is respectively small and large in relation to the wavelength, and the structure of the left-singular vectors is linked to the nonzero singular values of a Multi-Static Response (MSR) matrix whose elements are the *S*-parameters. Using simulations, we demonstrated the strengths and weaknesses of the MUSIC algorithm in detecting both small and extended anomalies.

1. Introduction

A key application of microwave tomographic imaging is the detection of small targets, such as tumors in early-stage breast cancer, from the measured scattered field or *S*-parameters. Generally, breast tumors have larger permittivity than the heterogeneities in normal tissue, which in principle should allow them to be distinguished from the background medium. This is known to be a difficult problem because of its intrinsic nonlinearity and ill-posedness. However, its potential importance to human life makes it of great interest to science.

A range of techniques aimed at detecting, localizing, and characterizing small anomalies through microwave tomographic imaging have therefore been proposed. The best known technique uses a Newton-type iteration method. Many studies [1–14] have investigated iteration-based techniques, and they have been successfully used to characterize, for example, the total number, location, and outline of small anomalies associated with breast cancer. However, the success of such iteration schemes is significantly dependent on the initial prediction, which must be close to the final outcome. Iteration schemes have other limitations, including slow convergence, the local minimizer problem, the difficulty of extension to multiple anomalies, and the need for appropriate regularization. A fast technique for detecting the exact or approximate location of a target remains elusive.

* First and corresponding author.
** Co-corresponding author.
E-mail addresses: parkwk@kookmin.ac.kr (W.-K. Park), hpkim0512@yonsei.ac.kr (H.P. Kim), reolee0122@etri.re.kr (K.-J. Lee), shs@etri.re.kr (S.-H. Son).

http://dx.doi.org/10.1016/j.jcp.2017.07.035
0021-9991/

The MUltiple SIgnal Classification (MUSIC) algorithm is a well-known non-iterative imaging technique for addressing inverse scattering. This technique has been applied to a range of problems, including the identification of small targets in free space [15–17], in inhomogeneous or anisotropic media [18–20], or buried in a half-space [21–23]; detection of internal corrosion [24]; eddy-current imaging [25]; imaging of crack-like defects [26–29] and arbitrarily shaped extended targets [6,30,31]; limited-view problem detection [32,33]; and biomedical imaging [34]. A clear description of MUSIC can be found in [35]. Studies have confirmed MUSIC to be a fast, stable, and effective technique for imaging of arbitrary unknown targets in full- and limited-view inverse scattering problems. However, to the best of our knowledge, it has not yet been applied in identifying unknown dielectric anomalies from measurements of scattered or S-parameters.

In this study, we used the MUSIC algorithm operated at a single frequency to identify the location and shape of small or extended dielectric anomalies from S-parameters collected by a limited number of dipole antennas. Our approach applied the Born approximation [3] or physical factorization of the multi-static response (MSR) matrix [30]. To confirm the practicality of this approach, we established a relationship between the imaging function of MUSIC and an infinite series of Bessel functions of integer order when the total number of dipole antennas is small. The mathematical structures of MUSIC have been shown to be applicable to full- and limited-view inverse scattering problems when a large number of directions of observation are available [27,32,33]. We performed numerical simulations to confirm the relationship, using synthetic data generated by the commercial CST studio suite, which is able to produce accurate electromagnetic data. Once the target has been imaged, its shape can be used as the initial prediction and can then be made more accurate by applying the Newton-type iteration algorithm, the level-set methodology, and optimization. As the initial estimate is close to the final outcome, the computational cost is also reduced.

The rest of this paper is organized as follows. In Section 2, the forward problem is briefly discussed and the basic concept of the S-parameter is introduced. Section 3 discusses the application of the MUSIC algorithm to anomaly detection. In Section 4, we introduce the experimental design used to investigate the relationship between the imaging function of MUSIC and an infinite series of Bessel functions of integer order, when using a limited number of dipole antennas, present the analysis of the imagining function, and discuss certain phenomena noted in our results. Section 5 presents our conclusions, gives an outline of current research, and makes proposals for future studies.

2. Forward problem and S-parameter

In this section, we briefly survey the three-dimensional forward problem in the case in which an anomaly $\mathcal{A}$ with a smooth boundary $\partial\mathcal{A}$ is surrounded by N-different dipole antennas located at $\mathbf{r}_n'$, $n = 1, 2, \cdots, N$ (see Fig. 1 for description). Throughout the study, we assumed all materials and anomalies to be non-magnetic, allowing them to be classified on the basis of their dielectric permittivity and electrical conductivity at a given angular frequency ω. To reflect this, we set the magnetic permeability to be constant at every location such that $\mu(\mathbf{r}) \equiv \mu_0$. If ε_0 and σ_0 respectively denote the initial permittivity and conductivity, then by analogy, $\varepsilon_{\mathcal{B}}$ and $\sigma_{\mathcal{B}}$ are respectively the background permittivity and conductivity, and $\varepsilon_{\mathcal{A}}$ and $\sigma_{\mathcal{A}}$ are respectively those of $\mathcal{A}$. The piecewise constant permittivity $\varepsilon(\mathbf{r})$ and conductivity $\sigma(\mathbf{r})$ can then be derived as follows:

$$\varepsilon(\mathbf{r}) = \begin{cases} \varepsilon_{\mathcal{A}} & \text{for} \quad \mathbf{r} \in \mathcal{A}, \\ \varepsilon_{\mathcal{B}} & \text{for} \quad \mathbf{r} \in \mathbb{R}^3 \backslash \overline{\mathcal{A}}, \end{cases} \quad \text{and} \quad \sigma(\mathbf{r}) = \begin{cases} \sigma_{\mathcal{A}} & \text{for} \quad \mathbf{r} \in \mathcal{A}, \\ \sigma_{\mathcal{B}} & \text{for} \quad \mathbf{r} \in \mathbb{R}^3 \backslash \overline{\mathcal{A}}. \end{cases}$$

Let $\mathbf{E}_{\text{inc}}(\mathbf{r}_n', \mathbf{r})$ be the incident electric field in a homogeneous medium due to a point current density $\mathbf{J}(\mathbf{r}_n', \mathbf{r})$ at $\mathbf{r}_n'$ with direction $\boldsymbol{\theta}$. Analogously, let $\mathbf{E}_{\text{tot}}(\mathbf{r}, \mathbf{r}_n')$ be the total field in the presence of $\mathcal{A}$. Then, $\mathbf{E}_{\text{tot}}(\mathbf{r}, \mathbf{r}_n')$ satisfies

$$\frac{1}{\mu_0}\left(\nabla \times \nabla \times \mathbf{E}_{\text{tot}}(\mathbf{r}, \mathbf{r}_n') - k^2 \mathbf{E}_{\text{tot}}(\mathbf{r}, \mathbf{r}_n')\right) = i\omega \mathbf{J}(\mathbf{r}_n', \mathbf{r})$$

with the transmission condition on the boundary $\partial\mathcal{A}$ and the following radiation (or open boundary) condition:

$$\lim_{|\mathbf{r}| \to \infty} \mathbf{r}\left(\nabla \times \mathbf{E}_{\text{tot}}(\mathbf{r}, \mathbf{r}_n') - ik\hat{\mathbf{r}} \times \mathbf{E}_{\text{tot}}(\mathbf{r}, \mathbf{r}_n')\right) = 0.$$

Here, $\hat{\mathbf{r}} = \mathbf{r}/|\mathbf{r}|$ and k denotes the wavenumber satisfying

$$k^2 = \omega^2 \mu_0 \left(\varepsilon_{\mathcal{B}} + i\frac{\sigma_{\mathcal{B}}}{\omega}\right).$$

The S-parameter (or scattering parameter) $S(a, b)$ is defined as the ratio of the output voltage (or reflected waves) at the ath antenna and the input voltage (or incident waves) at the bth antenna. In this paper, $S_{\text{scat}}(a, b)$ denotes the scattered field S-parameter obtained by subtracting the S-parameters for the total and incident fields. The presence of anomaly $\mathcal{A}$ then allows $S_{\text{scat}}(a, b)$ to be represented as follows [3]:

$$S_{\text{scat}}(a, b) \approx -\frac{k^2}{4i\omega\mu_0} \int_{\mathcal{A}} \left(\frac{\varepsilon(\mathbf{r})}{\varepsilon_0} - 1\right) \mathbf{E}_{\text{inc}}(\mathbf{r}_b', \mathbf{r}) \cdot \mathbf{E}_{\text{tot}}(\mathbf{r}, \mathbf{r}_a') d\mathbf{r}. \tag{1}$$

This representation will be critical in designing the MUSIC algorithm introduced in the next section. In this approach, we assume that the measurement of the scattering parameter is affected by anomaly $\mathcal{A}$ but not by the antennas.

3. MUSIC algorithm for anomaly detection

This section introduces the design of the proposed MUSIC algorithm for anomaly detection from measured scattered field S-parameters. We first consider the following MSR matrix $\mathbb{K}$ with transmitter number l and receiver number j:

$$\mathbb{K} = \begin{bmatrix} S_{\text{scat}}(1,1) & S_{\text{scat}}(1,2) & \cdots & S_{\text{scat}}(1,N) \\ S_{\text{scat}}(2,1) & S_{\text{scat}}(2,2) & \cdots & S_{\text{scat}}(2,N) \\ \vdots & \vdots & \ddots & \vdots \\ S_{\text{scat}}(N,1) & S_{\text{scat}}(N,2) & \cdots & S_{\text{scat}}(N,N) \end{bmatrix}. \tag{2}$$

Note that the wavelength λ corresponding to the wavenumber k is larger than the radius of anomaly $\mathcal{A}$. This problem can be viewed as that of imaging a small target and, by applying the Born approximation [3], formula (1) can be approximated as follows:

$$S_{\text{scat}}(j,l) \approx \frac{ik^2}{4\omega\mu_0} \int_{\mathcal{A}} \left(\frac{\varepsilon(\mathbf{r})}{\varepsilon_0} - 1 \right) \mathbf{E}_{\text{inc}}(\mathbf{r}'_l, \mathbf{r}) \cdot \mathbf{E}_{\text{inc}}(\mathbf{r}, \mathbf{r}'_j) d\mathbf{r}. \tag{3}$$

The range of $\mathbb{K}$ can then be determined from the span of

$$\mathbf{W}(\mathbf{r}) := \left[\mathbf{E}_{\text{inc}}(\mathbf{r}'_1, \mathbf{r}), \mathbf{E}_{\text{inc}}(\mathbf{r}'_2, \mathbf{r}), \cdots, \mathbf{E}_{\text{inc}}(\mathbf{r}'_N, \mathbf{r}) \right]^T \tag{4}$$

corresponding to $\mathcal{A}$.

To introduce the MUSIC algorithm, we first apply singular value decomposition (SVD) to $\mathbb{K}$, as follows:

$$\mathbb{K} = \mathbb{U}\mathbb{S}\mathbb{V}^* \approx \sum_{m=1}^{M} \tau_m \mathbf{U}_m \mathbf{V}_m^*,$$

where τ_m are the singular values, $\mathbf{U}_m$ and $\mathbf{V}_m$ are respectively the left and right singular vectors of $\mathbb{K}$, and $\mathbb{S}$ is a real nonnegative diagonal matrix with components $\tau_1, \tau_2, \cdots, \tau_N$ that satisfies

$$\tau_1 \geq \tau_2 \geq \cdots \geq \tau_M > 0.$$

For $m \geq M+1$, τ_m, could be very small. The first M columns of $\{\mathbf{U}_1, \mathbf{U}_2, \cdots, \mathbf{U}_M\}$ then provide an orthonormal basis for $\mathbb{K}$. This allows projection onto the null (or noise) subspace given explicitly by

$$\mathbb{P}_{\text{noise}} := \mathbb{I}_N - \sum_{m=1}^{M} \mathbf{U}_m \mathbf{U}_m^*. \tag{5}$$

There then exists $N_0 \in \mathbb{N}$ such that, for any $N \geq N_0$, the following statement holds (see [16,36]):

$$\mathbf{W}(\mathbf{r}) \in \text{Range}(\mathbb{K}) \quad \text{if and only if} \quad \mathbf{r} \in \mathcal{A}.$$

This means that if a point $\mathbf{r}$ satisfies $\mathbf{r} \in \mathcal{A}$, then $\mathbb{P}_{\text{noise}}(\mathbf{W}(\mathbf{r})) = 0$. The location of $\mathcal{A}$ can thus be identified by plotting

$$\mathcal{I}(\mathbf{r}) = \frac{1}{|\mathbb{P}_{\text{noise}}(\mathbf{W}(\mathbf{r}))|}. \tag{6}$$

The plot of $\mathcal{I}(\mathbf{r})$ is expected to exhibit peaks of large magnitude (in theory $+\infty$) at $\mathbf{r} \in \mathcal{A}$.

Remark 3.1 *(Application of asymptotic expansion formula).* Let α be the radius of $\mathcal{A}$, where α is smaller than λ. Then, based on the asymptotic expansion formula in [15], the total field $\mathbf{E}_{\text{tot}}(\mathbf{r}, \mathbf{r}'_n)$ satisfies

$$\mathbf{E}_{\text{tot}}(\mathbf{r}, \mathbf{r}'_n) \approx \mathbf{E}_{\text{inc}}(\mathbf{r}, \mathbf{r}'_n) + o(\alpha^3)$$

for all $n = 1, 2, \cdots, N$. This allows (3) to be approximated in a similar manner.

Table 1
Permittivities, conductivities, locations, and sizes of materials.

Target	Relative permittivity	Conductivity (S/m)	Location (mm)	Size (diameter)
$\mathcal{B}$: background	20	0.2	–	–
$\mathcal{S}$: skin-like (blue-colored)	35	0.3	–	2 mm thickness
$\mathcal{C}$: cylinder-like (cyan-colored)	15	0.5	(10, 20)	96 mm (enclosed by $\mathcal{S}$)
$\mathcal{T}$: tumor-like (red-colored)	55	1.2	(10, 30)	20 mm

Remark 3.2 *(Detection of an extended anomaly).* If α, the radius of $\mathcal{A}$, is larger than λ, then neither the Born approximation nor the asymptotic expansion formula introduced above can be applied. Note that $\mathbb{K}$ can be decomposed as

$$\mathbb{K} = \frac{ik^2}{4\omega\mu_0} \int_{\mathcal{A}} \left(\frac{\varepsilon(\mathbf{r})}{\varepsilon_0} - 1 \right) \mathbb{E}(\mathbf{r}) \mathbb{F}(\mathbf{r}) d\mathbf{r}, \tag{7}$$

where $\mathbb{E}(\mathbf{r})$ and $\mathbb{F}(\mathbf{r})$ are

$$\mathbb{E}(\mathbf{r}) = \left[\mathbf{E}_{\text{inc}}(\mathbf{r}'_1, \mathbf{r}), \mathbf{E}_{\text{inc}}(\mathbf{r}'_2, \mathbf{r}), \cdots, \mathbf{E}_{\text{inc}}(\mathbf{r}'_N, \mathbf{r}) \right]^T \quad \text{and} \quad \mathbb{F}(\mathbf{r}) = \left[\mathbf{E}_{\text{tot}}(\mathbf{r}, \mathbf{r}'_1), \mathbf{E}_{\text{tot}}(\mathbf{r}, \mathbf{r}'_2), \cdots, \mathbf{E}_{\text{tot}}(\mathbf{r}, \mathbf{r}'_N) \right],$$

respectively.

Formula (7) is a factorization of the $\mathbb{K}$ that separates the known information about the incoming wave from unknown information. The range of $\mathbb{K}$ is then determined on the basis of the span of the $\mathbb{E}(\mathbf{r})$ that corresponds to $\mathcal{A}$, so that a signal subspace can be defined using the set of remaining left-singular vectors of $\mathbb{K}$. MUSIC can therefore retrieve an outline of the shape of $\mathcal{A}$. For a more detailed discussion and analysis of simulation results, see [30].

4. Experimental setup, mathematical analysis, and discussion of simulation results

In this section, we introduce the test configuration used in our simulations, present an analysis of the imaging function, and discuss some phenomena identified in our results.

4.1. Experimental setup

Our experimental simulation used 16 dipole antennas and applied a frequency of $f = 1$ GHz, or $\omega = 2\pi f \times 10^9 = 2\pi \times 10^9$ Rad/s angular frequency. As noted above, none of the materials were magnetic, so parameter $\mu(\mathbf{r})$ was set to $\mu(\mathbf{r}) \equiv 4 \times 10^{-7}\pi$ and the initial permittivity ε_0 to $\varepsilon_0 = 8.854187818 \times 10^{-12}$. The relative permittivity and conductivity were respectively set to $\varepsilon_{\mathcal{B}} = 20$ and $\sigma_{\mathcal{B}} = 0.2$S/m. The relative permittivity, conductivity, location, and size of each anomaly is given in Table 1, while Fig. 1 shows the test configurations. In these configurations, the wavenumber k was $k \approx 94.1038 + 8.3904i$, so that the wavelength λ was larger than the diameter of $\mathcal{T}$ and smaller than that of $\mathcal{C}$. The elements $S_{\text{scat}}(j, l)$ of $\mathbb{K}$ were generated using CST studio with a background of $\mathcal{B}$ in Examples 4.1, 4.2, and 4.3, and $\mathcal{B} \cup \mathcal{C} \cup \mathcal{S}$ in Example 4.4 introduced in Section 4.3. In this paper, we set $\mathcal{T}$ is a sphere with small radius and $\mathcal{C}$ is a cylinder with height 200 mm.

Remark 4.1 *(Polarization).* Since the height of $\mathcal{C}$ is long enough, $\mathcal{C}$ can be regarded as an infinitely long cylindrical object with a thickness close to zero. Since the antennas were omnidirectional and arranged perpendicular to the z-axis, based on mathematical treatment of the scattering of time-harmonic electromagnetic waves from thin infinitely long cylindrical obstacles (see [37] for instance), $\mathbf{W}(\mathbf{r})$ of (4) could be rewritten in the following normalized form:

$$\mathbf{W}(\mathbf{r}) = \frac{\left[H_0^{(2)}(k|\mathbf{r}'_1 - \mathbf{r}|), H_0^{(2)}(k|\mathbf{r}'_2 - \mathbf{r}|), \cdots, H_0^{(2)}(k|\mathbf{r}'_N - \mathbf{r}|) \right]^T}{\left| \sum_{n=1}^{N} H_0^{(2)}(k|\mathbf{r}'_n - \mathbf{r}|) \overline{H_0^{(2)}(k|\mathbf{r}'_n - \mathbf{r}|)} \right|^{1/2}}.$$

4.2. Mathematical analysis: expression of infinite series of Bessel functions of integer order

We next analyzed the imaging function (6) by expressing an infinite series of Bessel functions of integer order. This was done for a case in which there is only one anomaly $\mathcal{A}$, λ is larger than the radius of $\mathcal{A}$, and $\mathcal{A}$ is far from antennas $\mathbf{r}'_n$, for $n = 1, 2, \cdots, N$ so that $|\mathbf{r}'_n - \mathbf{r}_{\mathcal{A}}| \gg 0.25/k$. There is only one nonzero singular value, and by applying (3) and the asymptotic form of the Hankel function

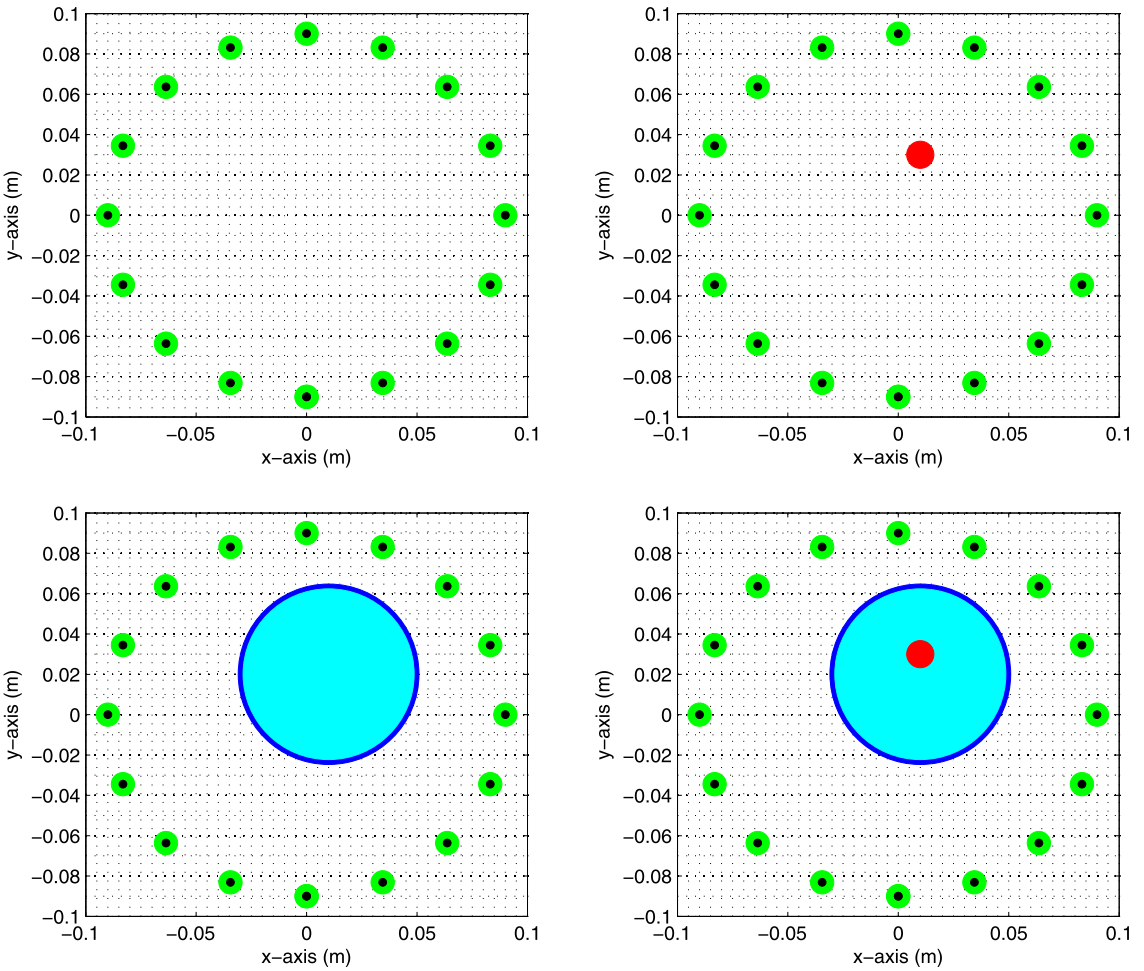

Fig. 1. Description of test configurations.

$$H_0^{(2)}(k|\mathbf{r}'_n - \mathbf{r}_{\mathcal{A}}|) = \frac{1+i}{4\sqrt{k\pi}} \frac{e^{ik|\mathbf{r}'_n|}}{\sqrt{|\mathbf{r}'_n|}} \exp\left(-ik\frac{\mathbf{r}'_n}{|\mathbf{r}'_n|}\cdot\mathbf{r}_{\mathcal{A}}\right) + o\left(\frac{1}{\sqrt{|\mathbf{r}'_n|}}\right), \tag{8}$$

it can be easily seen that the first left-singular vector $\mathbf{U}_1$ of the MSR matrix $\mathbb{K}$ takes the form

$$\mathbf{U}_1 \approx \frac{\mathbf{W}(\mathbf{r}_{\mathcal{A}})}{|\mathbf{W}(\mathbf{r}_{\mathcal{A}})|} = \frac{1}{\sqrt{N}}\left[\exp(-ik\hat{\mathbf{r}}'_1\cdot\mathbf{r}_{\mathcal{A}}), \exp(-ik\hat{\mathbf{r}}'_2\cdot\mathbf{r}_{\mathcal{A}}), \cdots, \exp(-ik\hat{\mathbf{r}}'_N\cdot\mathbf{r}_{\mathcal{A}})\right]^T, \tag{9}$$

where $\hat{\mathbf{r}}'_n = \mathbf{r}'_n/|\mathbf{r}'_n|$ for $n = 1, 2, \cdots, N$.

We first assume that the searing point $\mathbf{r}$ is far from antennas $\mathbf{r}'_n$, such that $k|\mathbf{r}'_n - \mathbf{r}| \gg 0.25$. Then, applying (8) and (9), we can examine. Then, we can evaluate

$$\mathbb{P}_{\text{noise}}(\mathbf{W}(\mathbf{r})) = \left(\mathbb{I} - \mathbb{U}_1\mathbb{U}_1^*\right)\mathbf{W}(\mathbf{r}) = \frac{1}{\sqrt{N}}\begin{bmatrix}\exp(-ik\hat{\mathbf{r}}'_1\cdot\mathbf{r})\\ \exp(-ik\hat{\mathbf{r}}'_2\cdot\mathbf{r})\\ \vdots\\ \exp(-ik\hat{\mathbf{r}}'_N\cdot\mathbf{r})\end{bmatrix} - \frac{\mathbf{H}}{\sqrt{N}},$$

where $\mathbf{H} \in \mathbb{C}^{N\times 1}$ is

$$\mathbf{H} = \begin{bmatrix} \exp(-ik\hat{\mathbf{r}}_1'\cdot\mathbf{r}) + \sum_{n\in\mathbb{N}_1}\exp\Big(-ik(\hat{\mathbf{r}}_1'\cdot\mathbf{r}_{\mathcal{A}} - \hat{\mathbf{r}}_n'\cdot(\mathbf{r}-\mathbf{r}_{\mathcal{A}}))\Big) \\ \exp(-ik\hat{\mathbf{r}}_2'\cdot\mathbf{r}) + \sum_{n\in\mathbb{N}_2}\exp\Big(-ik(\hat{\mathbf{r}}_2'\cdot\mathbf{r}_{\mathcal{A}} - \hat{\mathbf{r}}_n'\cdot(\mathbf{r}-\mathbf{r}_{\mathcal{A}}))\Big) \\ \vdots \\ \exp(-ik\hat{\mathbf{r}}_N'\cdot\mathbf{r}) + \sum_{n\in\mathbb{N}_N}\exp\Big(-ik(\hat{\mathbf{r}}_N'\cdot\mathbf{r}_{\mathcal{A}} - \hat{\mathbf{r}}_n'\cdot(\mathbf{r}-\mathbf{r}_{\mathcal{A}}))\Big) \end{bmatrix}.$$

Here, the set $\mathbb{N}_h$ is defined as follows: for $h = 1, 2, \cdots, N$,

$$\mathbb{N}_h := \{1, 2, \cdots, N\}\backslash\{h\}.$$

Since

$$\exp(-ik\hat{\mathbf{r}}_h'\cdot\mathbf{r}) = \exp(-ik\hat{\mathbf{r}}_h'\cdot\mathbf{r}_{\mathcal{A}})\exp(-ik\hat{\mathbf{r}}_h'\cdot(\mathbf{r}-\mathbf{r}_{\mathcal{A}})),$$

for $h = 1, 2, \cdots, N$, we can evaluate

$$\frac{1}{N}\left\{\exp(-ik\hat{\mathbf{r}}_h'\cdot\mathbf{r}) + \sum_{n\in\mathbb{N}_h}\exp\Big(-ik(\hat{\mathbf{r}}_h'\cdot\mathbf{r}_{\mathcal{A}} + \hat{\mathbf{r}}_n'\cdot(\mathbf{r}-\mathbf{r}_{\mathcal{A}}))\Big)\right\} = \exp(-ik\hat{\mathbf{r}}_h'\cdot\mathbf{r}_{\mathcal{A}})\frac{1}{N}\sum_{n=1}^{N}\exp(-ik\hat{\mathbf{r}}_n'\cdot(\mathbf{r}-\mathbf{r}_{\mathcal{A}})),$$

and we consequently obtain

$$\mathbb{P}_{\text{noise}}(\mathbf{W}(\mathbf{r})) = \frac{1}{\sqrt{N}}\begin{bmatrix} \exp(-ik\hat{\mathbf{r}}_1'\cdot\mathbf{r}) - \exp(-ik\hat{\mathbf{r}}_1'\cdot\mathbf{r}_{\mathcal{A}})\frac{1}{N}\sum_{n=1}^{N}\exp(-ik\hat{\mathbf{r}}_n'\cdot(\mathbf{r}-\mathbf{r}_{\mathcal{A}})) \\ \exp(-ik\hat{\mathbf{r}}_2'\cdot\mathbf{r}) - \exp(-ik\hat{\mathbf{r}}_2'\cdot\mathbf{r}_{\mathcal{A}})\frac{1}{N}\sum_{n=1}^{N}\exp(-ik\hat{\mathbf{r}}_n'\cdot(\mathbf{r}-\mathbf{r}_{\mathcal{A}})) \\ \vdots \\ \exp(-ik\hat{\mathbf{r}}_N'\cdot\mathbf{r}) - \exp(-ik\hat{\mathbf{r}}_N'\cdot\mathbf{r}_{\mathcal{A}})\frac{1}{N}\sum_{n=1}^{N}\exp(-ik\hat{\mathbf{r}}_n'\cdot(\mathbf{r}-\mathbf{r}_{\mathcal{A}})) \end{bmatrix}.$$

Hence, we can observe that

$$|\mathbb{P}_{\text{noise}}(\mathbf{W}(\mathbf{r}))|^2 = \mathbb{P}_{\text{noise}}(\mathbf{W}(\mathbf{r}))\cdot\overline{\mathbb{P}_{\text{noise}}(\mathbf{W}(\mathbf{r}))} = \frac{1}{N}\sum_{n=1}^{N}\Big(1 - (\Lambda_1 + \overline{\Lambda}_1) + (\Lambda_2\overline{\Lambda}_2)\Big),$$

where

$$\Lambda_1 := \exp(-ik\hat{\mathbf{r}}_n'\cdot(\mathbf{r}-\mathbf{r}_{\mathcal{A}}))\frac{1}{N}\sum_{s=1}^{N}\exp(-ik\hat{\mathbf{r}}_s'\cdot(\mathbf{r}-\mathbf{r}_{\mathcal{A}}))$$

$$\Lambda_2 := \exp(-ik\hat{\mathbf{r}}_n'\cdot\mathbf{r}_{\mathcal{A}})\frac{1}{N}\sum_{s=1}^{N}\exp(-ik\hat{\mathbf{r}}_s'\cdot(\mathbf{r}-\mathbf{r}_{\mathcal{A}})).$$

Now, let us consider the polar coordinate $\hat{\mathbf{r}}_n' = [\cos\theta_n', \sin\theta_n']^T$ and $\mathbf{r}-\mathbf{r}_{\mathcal{A}} = |\mathbf{r}-\mathbf{r}_{\mathcal{A}}|[\cos\phi_{\mathcal{A}}, \sin\phi_{\mathcal{A}}]^T$. Let $\mathbb{Z}^* := \mathbb{Z}\cup\{-\infty, +\infty\}$. Then, by applying Jacobi–Anger expansion,

$$\exp(ix\cos\theta) = J_0(x) + \sum_{\nu\in\mathbb{Z}^*\backslash\{0\}} i^{\nu}J_{\nu}(x)\exp(i\nu\theta), \tag{10}$$

we derive

$$\frac{1}{N}\sum_{n=1}^{N}\Lambda_1 = \frac{1}{N}\sum_{n=1}^{N}\left(J_0(k|\mathbf{r}-\mathbf{r}_{\mathcal{A}}|)+\sum_{\nu\in\mathbb{Z}^*\setminus\{0\}} i^{\nu}J_{\nu}(k|\mathbf{r}-\mathbf{r}_{\mathcal{A}}|)\exp(i\nu(\theta_n'-\phi_{\mathcal{A}}))\right)$$
$$\times\frac{1}{N}\sum_{s=1}^{N}\left(J_0(k|\mathbf{r}-\mathbf{r}_{\mathcal{A}}|)+\sum_{\nu\in\mathbb{Z}^*\setminus\{0\}} i^{\nu}J_{\nu}(k|\mathbf{r}-\mathbf{r}_{\mathcal{A}}|)\exp(i\nu(\theta_s'-\phi_{\mathcal{A}}))\right)$$
$$= J_0(k|\mathbf{r}-\mathbf{r}_{\mathcal{A}}|)^2+\frac{1}{N^2}\left(\sum_{n=1}^{N}\sum_{\nu\in\mathbb{Z}^*\setminus\{0\}} i^{\nu}J_{\nu}(k|\mathbf{r}-\mathbf{r}_{\mathcal{A}}|)\exp(i\nu(\theta_n'-\phi_{\mathcal{A}}))\right)^2.$$

Here, $J_\nu(x)$ denotes a Bessel function of order ν of the first kind. Thus

$$\frac{1}{N}\sum_{n=1}^{N}(\Lambda_1+\overline{\Lambda}_1) = 2J_0(k|\mathbf{r}-\mathbf{r}_{\mathcal{A}}|)^2+\frac{2}{N^2}\mathrm{Re}\left(\sum_{n=1}^{N}\sum_{\nu\in\mathbb{Z}^*\setminus\{0\}} i^{\nu}J_{\nu}(k|\mathbf{r}-\mathbf{r}_{\mathcal{A}}|)\exp(i\nu(\theta_n'-\phi_{\mathcal{A}}))\right)^2, \tag{11}$$

where $\mathrm{Re}(\mathbf{c})$ denotes the real part of $\mathbf{c}\in\mathbb{C}$.

Next, for $\mathbf{a}, \mathbf{b}_n \in \mathbb{C}$ with $|\mathbf{a}|=1$,

$$\left(\mathbf{a}\sum_{n=1}^{N}\mathbf{b}_n\right)\left(\overline{\mathbf{a}}\sum_{s=1}^{N}\overline{\mathbf{b}}_s\right) = \mathrm{Re}\left(\sum_{n=1}^{N}\mathbf{b}_n\right)^2,$$

and applying (10) again, we derive

$$\frac{1}{N}\sum_{n=1}^{N}\Lambda_2\overline{\Lambda}_2 = \frac{1}{N^2}\mathrm{Re}\left(\sum_{s=1}^{N}\exp(-ik\hat{\mathbf{r}}_s'\cdot(\mathbf{r}-\mathbf{r}_{\mathcal{A}}))\right)^2$$
$$= \frac{1}{N^2}\mathrm{Re}\left\{\sum_{s=1}^{N}\left(J_0(k|\mathbf{r}-\mathbf{r}_{\mathcal{A}}|)+\sum_{\nu\in\mathbb{Z}^*\setminus\{0\}} i^{\nu}J_{\nu}(k|\mathbf{r}-\mathbf{r}_{\mathcal{A}}|)\exp(i\nu(\theta_s'-\phi_{\mathcal{A}}))\right)\right\}^2 \tag{12}$$
$$= J_0(k|\mathbf{r}-\mathbf{r}_{\mathcal{A}}|)^2+\frac{1}{N^2}\mathrm{Re}\left(\sum_{n=1}^{N}\sum_{\nu\in\mathbb{Z}^*\setminus\{0\}} i^{\nu}J_{\nu}(k|\mathbf{r}-\mathbf{r}_{\mathcal{A}}|)\exp(i\nu(\theta_n'-\phi_{\mathcal{A}}))\right)^2.$$

Combining (11) and (12), we obtain

$$|\mathbb{P}_{\mathrm{noise}}(\mathbf{W}(\mathbf{r}))|^2 = 1-J_0(k|\mathbf{r}-\mathbf{r}_{\mathcal{A}}|)^2-\frac{1}{N^2}\mathrm{Re}\left(\sum_{n=1}^{N}\sum_{\nu\in\mathbb{Z}^*\setminus\{0\}} i^{\nu}J_{\nu}(k|\mathbf{r}-\mathbf{r}_{\mathcal{A}}|)\exp(i\nu(\theta_n'-\phi_{\mathcal{A}}))\right)^2.$$

Next, we assume that the searing point $\mathbf{r}$ is close to the antenna $\mathbf{r}_n'$. Then, since

$$|H_0^{(2)}(k|\mathbf{r}_n'-\mathbf{r}|)| \longrightarrow +\infty \quad \text{as} \quad \mathbf{r}\longrightarrow\mathbf{r}_n',$$

the value of $|\mathbb{P}_{\mathrm{noise}}(\mathbf{W}(\mathbf{r}))|$ will be sufficiently large, and the value of $\mathcal{I}(\mathbf{r})$ will be small in the neighborhood of $\mathbf{r}_n'$. This yields the following.

Theorem 4.1. *Assume that the wavenumber k is sufficiently large and that the number of antennas N is small. Let $\hat{\mathbf{r}}_n' = [\cos\theta_n', \sin\theta_n']^T$ and $\mathbf{r}-\mathbf{r}_{\mathcal{A}} = |\mathbf{r}-\mathbf{r}_{\mathcal{A}}|[\cos\phi_{\mathcal{A}}, \sin\phi_{\mathcal{A}}]^T$. Then, $\mathcal{I}(\mathbf{r})$ can be represented as follows: if $\mathbf{r}$ is far from $\mathbf{r}_n'$,*

$$\mathcal{I}(\mathbf{r}) = \left(1-J_0(k|\mathbf{r}-\mathbf{r}_{\mathcal{A}}|)^2-\frac{1}{N^2}\mathcal{D}(\mathbf{r},\mathbf{r}_{\mathcal{A}},\mathbf{r}_n',k)\right)^{-1/2}, \tag{13}$$

where

$$\mathcal{D}(\mathbf{r},\mathbf{r}_{\mathcal{A}},\mathbf{r}_n',k) := \mathrm{Re}\left(\sum_{n=1}^{N}\sum_{\nu\in\mathbb{Z}^*\setminus\{0\}} i^{\nu}J_{\nu}(k|\mathbf{r}-\mathbf{r}_{\mathcal{A}}|)\exp(i\nu(\theta_n'-\phi_{\mathcal{A}}))\right)^2.$$

Conversely, if $\mathbf{r}$ is close to $\mathbf{r}_n'$ for some n, then the value of $\mathcal{I}(\mathbf{r})$ is sufficiently small.

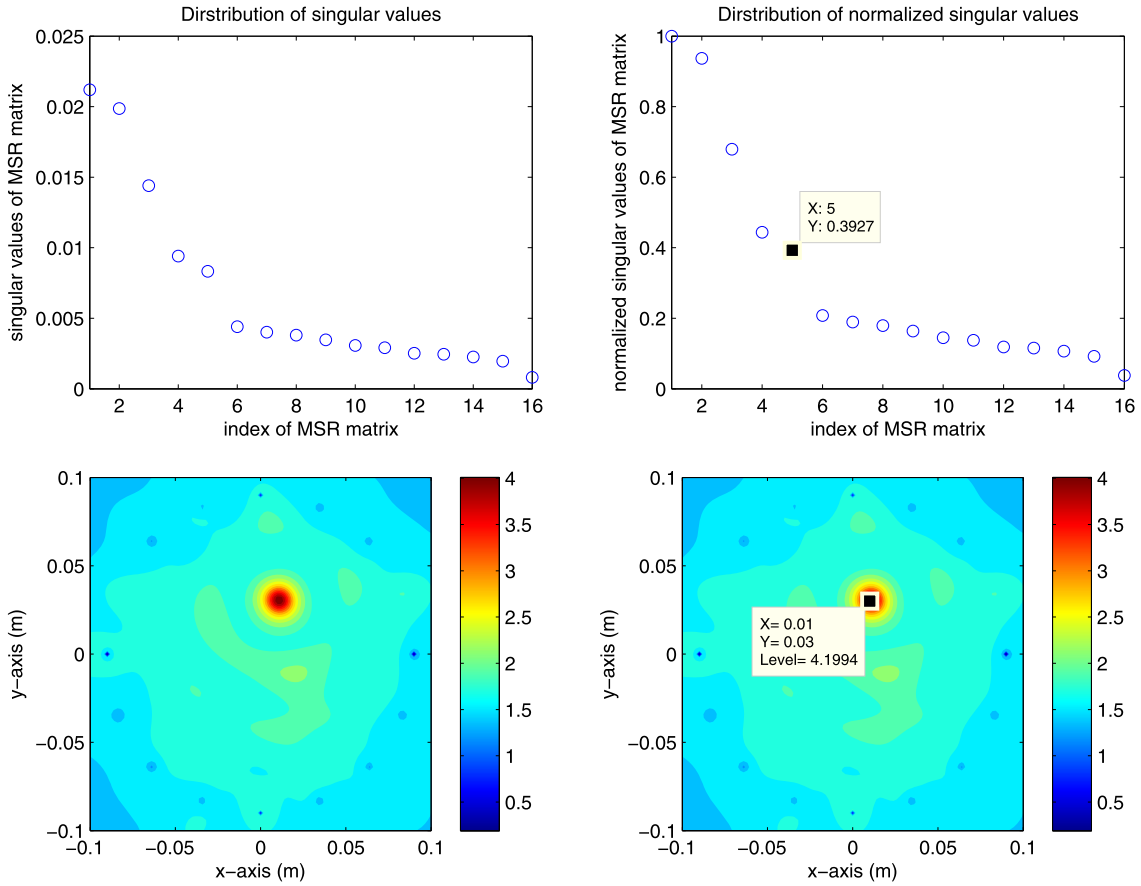

Fig. 2. (Example 4.1) Distribution of singular values (top, left) and normalized singular values (top, right) of $\mathbb{K}$, map of $\mathcal{I}(\mathbf{r})$ (bottom, left), and identified location (bottom, right) for $f = 1$ GHz frequency when anomaly is $\mathcal{T}$.

Remark 4.2. If the total number of antennas is sufficiently large then, we can say that

$$\frac{1}{N^2}\mathcal{D}(\mathbf{r}, \mathbf{r}_{\mathcal{A}}, \mathbf{r}'_n, k) \longrightarrow 0.$$

Therefore, (13) becomes

$$\mathcal{I}(\mathbf{r}) \approx \left(1 - J_0(k|\mathbf{r} - \mathbf{r}_{\mathcal{A}}|)^2\right)^{-1/2}.$$

This result is same as that derived in [27].

4.3. Simulation results and discussion

We now present our simulation results and use them to examine the effectiveness of MUSIC and to support the mathematical structure derived in Theorem 4.1. The search domain was assumed to be a $[-0.1, 0.1] \times [-0.1, 0.1]$ m^2 square and the step size of $\mathbf{r}$ to be of the order of 0.002 m.

Remark 4.3 *(Discrimination of nonzero singular values).* If we assume that only one small anomaly $\mathcal{T}$ exists, the number of nonzero singular values, M, of $\mathbb{K}$ must in theory equal 1. However, this is not true in real applications (nonzero singular values of 5 and 3 can be respectively seen in Figs. 2 and 5). Furthermore, the selection of nonzero singular values is extremely challenging when the anomaly is $\mathcal{C} \cup \mathcal{S}$, as in Fig. 3. For proper detection, therefore, the threshold must be set carefully to enable discrimination of nonzero singular values of $\mathbb{K}$. In this study, motivated from [28,29], we adopted the 0.4-thresholding technique (choosing first m singular values τ_m such that $\tau_m/\tau_1 \geq 0.4$) to discriminate nonzero singular value.

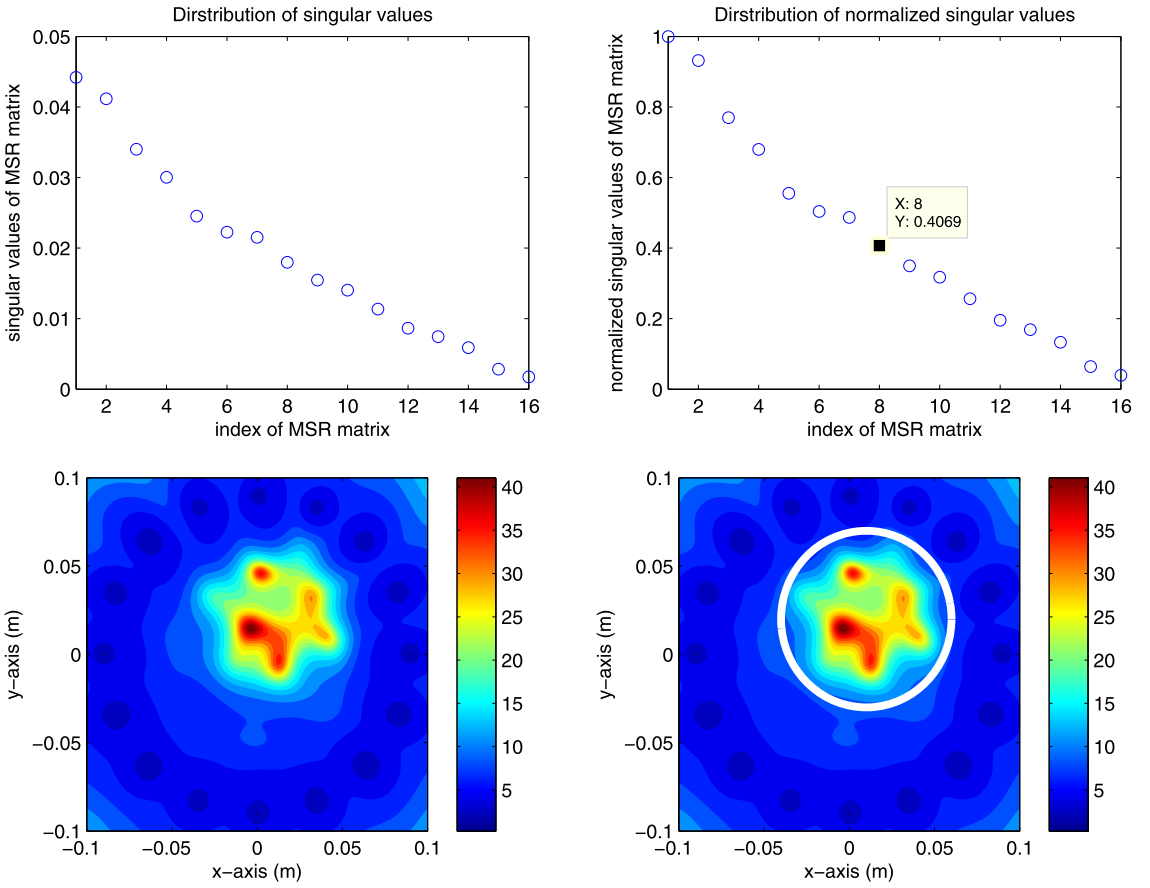

Fig. 3. (Example 4.2) Same as Fig. 2 except that the anomaly is $\mathcal{C} \cup \mathcal{S}$. White circle describes $\mathcal{S}$.

Example 4.1 *(Imaging of a small anomaly: Fig. 2).* We first considered the imaging of a small anomaly $\mathcal{T}$. In this example, the first five singular values were used to define the noise subspace. As expected, the location of $\mathcal{T}$ was retrieved with great accuracy, and the value of $\mathcal{I}(\mathbf{r})$ at each antenna was small, as predicted theoretically. Large-magnitude peaks appeared in the map of $\mathcal{T}$ at some of the antennas.

Example 4.2 *(Imaging of large anomaly: Fig. 3).* We next analyzed the imaging of a large anomaly $\mathcal{C}$ enclosed by $\mathcal{S}$, so that $\mathcal{C} \cup \mathcal{S}$. In this case, the first eight singular values were used for defining the noise subspace. Since the radius of $\mathcal{C}$ was larger than the wavelength, the Born approximation could not be applied and the simulation results did not match the result given by Theorem 4.1. Although it was impossible to identify the full shape of $\mathcal{C} \cup \mathcal{S}$, the existence of a large anomaly was recognized. By adopting this anomaly as the initial prediction, we believe that it would be possible to retrieve almost the complete shape of $\mathcal{C} \cup \mathcal{S}$ by applying Newton-type methods or a level-set strategy [4]. A similar phenomenon was discussed in [30].

Example 4.3 *(Imaging of a small anomaly embedded in a large anomaly: Fig. 4).* Next, we considered the imaging of a small anomaly $\mathcal{T}$ completely embedded in a larger anomaly so that $\mathcal{C} \cup \mathcal{S}$. This is common in the biomedical imaging used, for example, in early breast cancer detection. We selected the first eight singular values to define the noise subspace. As in Example 4.2, the simulation results did not match those derived from Theorem 4.1. Since the outline retrieved was that of $\mathcal{C} \cup \mathcal{S}$, it was impossible to detect $\mathcal{T}$, and no information on $\mathcal{T}$ could be retrieved. An effective algorithm for solving this problem is needed.

Example 4.4 *(Imaging of a small anomaly embedded in a large anomaly: Fig. 5).* Finally, we reconsidered the imaging of $\mathcal{T}$ hidden inside $\mathcal{C} \cup \mathcal{S}$. In contrast with Example 4.3, the S-parameters were generated against a background of $\mathcal{B} \cup \mathcal{C} \cup \mathcal{S}$. As in Example 4.1, it was possible to discriminate nonzero singular values of $\mathbb{K}$, but this time the first three singular values were used to generate the noise subspace. As in Example 4.1, the existence of $\mathcal{T}$ was recognized and large-magnitude peaks were observed at some of the antennas.

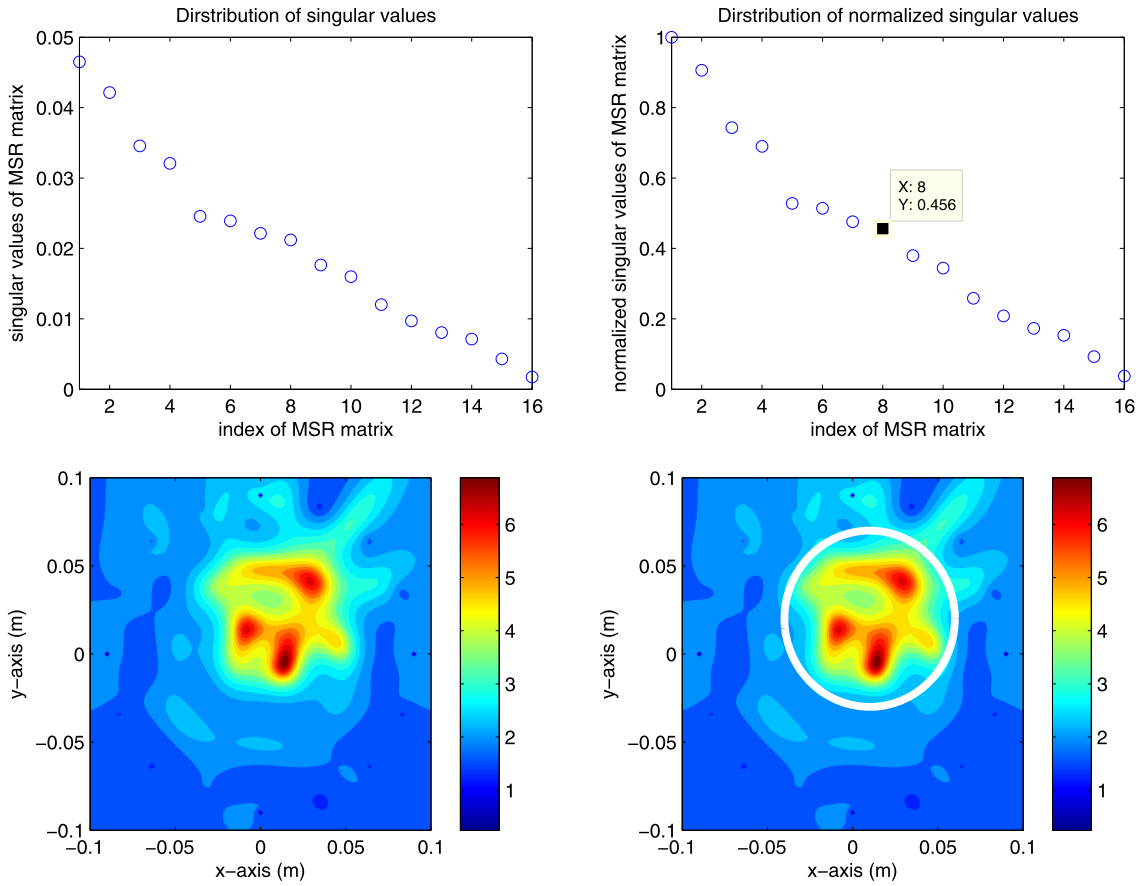

Fig. 4. (Example 4.3) Same as Fig. 2 except that the anomaly $\mathcal{T}$ is embedded in $\mathcal{C} \cup \mathcal{S}$. White circle describes $\mathcal{S}$.

5. Conclusions

This study considered the use of a MUSIC-type algorithm for imaging of small and extended anomalies in an inverse scattering problem, based on microwave scanning. We applied the Born approximation, a structure of singular vectors linked to the nonzero singular values of the collected MSR matrix, and the asymptotic properties of the Hankel function and successfully demonstrated that a MUSIC-type imaging function can be represented as an infinite series of integer-order Bessel functions of the first kind. The investigation elucidated a number of properties of MUSIC when applied to microwave imaging.

Simulations were conducted with synthetic data computed using CST studio, and the pros and cons of using MUSIC for the imaging of small and large anomalies were discussed. The results confirmed that MUSIC is an effective non-iterative technique that can be applied to microwave imaging but that its application is currently restricted to the detection of small anomalies. Further improvements would include imaging of extended anomalies and of small anomalies completely concealed within a larger anomaly with a homogeneous background. Relevant previous studies include [7,8,38,39]. Furthermore, we believe that MUSIC-type imaging considered herein can be improved by using multipole expansion technique considered in [40]. Performing related mathematical analysis and numerical simulation will be the forthcoming work.

When applied to an extended anomaly, although the full shape was not revealed, the results provided a good initial prediction for use in level-set evolution or with a standard iterative algorithm [4,6,9,41–44].

Acknowledgements

W.-K. Park would like to acknowledge professor Dominique Lesselier for his valuable advices. The authors are very grateful to professor Jin Keun Seo for his most useful discussions. The constructive comments of two anonymous reviewers are also acknowledged. Part of this work was done while W.-K. Park was visiting Génie électrique et électronique de Paris (GeePs), CentraleSupélec, Université Paris-Sud. This research was supported by the Basic Science Research Program through the National Research Foundation of Korea (NRF) funded by the Ministry of Education (No. NRF-2015R1A5A1009350 and 2017R1D1A1A09000547) and Electronics and Telecommunications Research Institute (ETRI) grant funded by the Korean government (No. 17ZR1400).

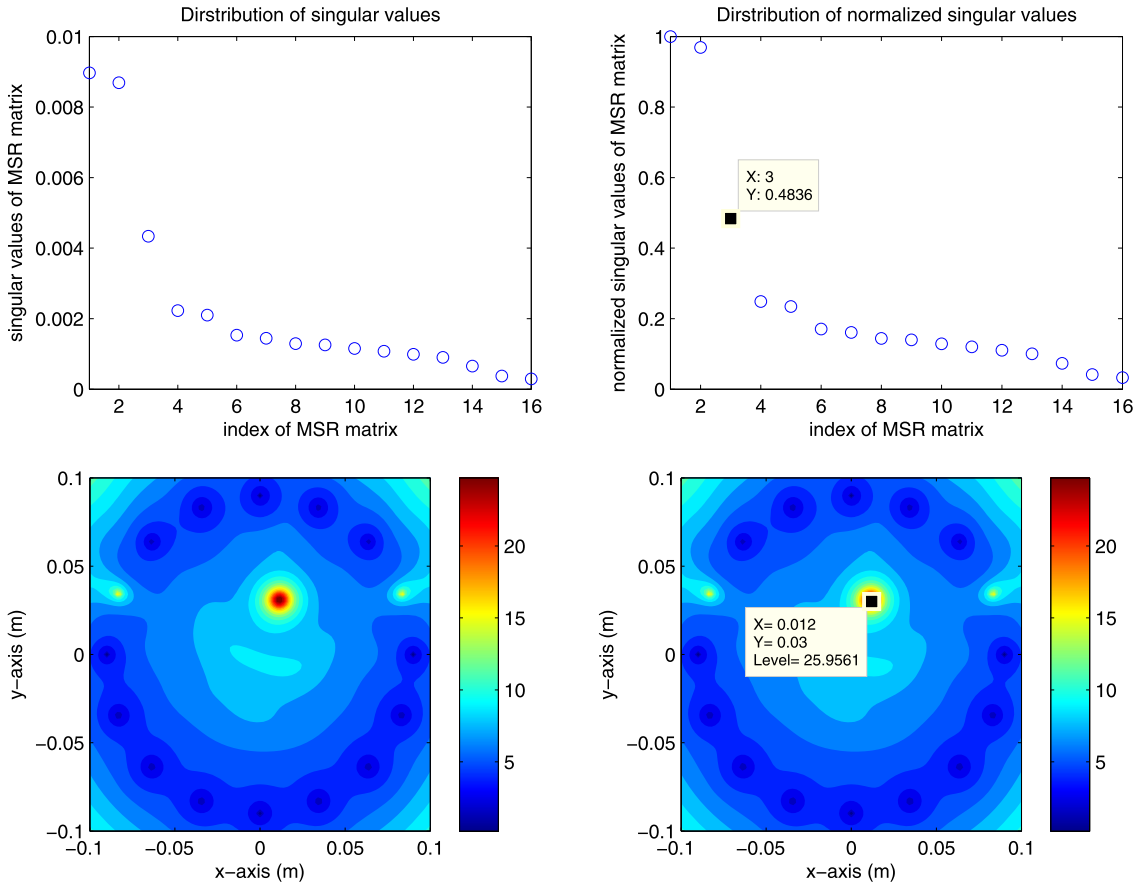

Fig. 5. (Example 4.4) Same as Fig. 2 except that the background S-parameter is generated when the background is $\mathcal{B} \cup \mathcal{C} \cup \mathcal{S}$.

References

[1] M. Burger, A level set method for inverse problems, Inverse Probl. 17 (2001) 1327–1356.
[2] Q. Fang, S.A. Carp, J. Selb, G. Boverman, Q. Zhang, D.B. Kopans, R.H. Moore, E.L. Miller, D.H. Brooks, D.A. Boas, Combined optical imaging and mammography of the healthy breast: optical contrast derived from breast structure and compression, IEEE Trans. Med. Imaging 28 (2009) 30–42.
[3] M. Haynes, J. Stang, M. Moghaddam, Real-time microwave imaging of differential temperature for thermal therapy monitoring, IEEE Trans. Biomed. Eng. 61 (2014) 1787–1797.
[4] O. Dorn, D. Lesselier, Level set methods for inverse scattering, Inverse Probl. 22 (2006) R67–R131.
[5] O. Dorn, E.L. Miller, C.M. Rappaport, A shape reconstruction method for electromagnetic tomography using adjoint fields and level sets, Inverse Probl. 16 (2000) 1119–1156.
[6] S. Hou, K. Sølna, H. Zhao, Imaging of location and geometry for extended targets using the response matrix, J. Comput. Phys. 199 (2004) 317–338.
[7] N. Irishina, O. Dorn, M. Moscoso, A level set evolution strategy in microwave imaging for early breast cancer detection, Comput. Math. Appl. 56 (2008) 607–618.
[8] N. Irishina, M. Moscoso, O. Dorn, Microwave imaging for early breast cancer detection using a shape-based strategy, IEEE Trans. Biomed. Eng. 56 (2009) 1143–1153.
[9] F. Santosa, A level-set approach for inverse problems involving obstacles, ESAIM Control Optim. Calc. Var. 1 (1996) 17–33.
[10] J.D. Shea, P. Kosmas, S.C. Hagness, B.D.V. Veen, Three-dimensional microwave imaging of realistic numerical breast phantoms via a multiple-frequency inverse scattering technique, Med. Phys. 37 (2010) 4210–4226.
[11] J.D. Shea, P. Kosmas, B.D.V. Veen, S.C. Hagness, Contrast-enhanced microwave imaging of breast tumors: a computational study using 3-D realistic numerical phantoms, Inverse Probl. 26 (2010) 074009.
[12] G. Ventura, J.X. Xu, T. Belytschko, A vector level set method and new discontinuity approximations for crack growth by EFG, Int. J. Numer. Methods Eng. 54 (2002) 923–944.
[13] G.-J. Yi, W.-G. Kang, H.-J. Kim, S.-I. Jeon, J.-K. Pack, A prototype system for early-stage breast cancer detection, J. Electr. Eng. Sci. 15 (2015) 158–166.
[14] S.H. Zainud-Deen, W.M. Hassen, E.M. Ali, K.H. Awadalla, H.A. Sharshar, Breast cancer detection using a hybrid finite difference frequency domain and particle swarm optimization techniques, Prog. Electromagn. Res. B 3 (2008) 35–46.
[15] H. Ammari, E. Iakovleva, D. Lesselier, G. Perrusson, MUSIC type electromagnetic imaging of a collection of small three-dimensional inclusions, SIAM J. Sci. Comput. 29 (2007) 674–709.
[16] H. Ammari, H. Kang, Reconstruction of Small Inhomogeneities from Boundary Measurements, Lect. Notes Math., vol. 1846, Springer-Verlag, Berlin, 2004.
[17] X. Chen, Y. Zhong, MUSIC electromagnetic imaging with enhanced resolution for small inclusions, Inverse Probl. 25 (2009) 015008.
[18] A. Kirsch, The MUSIC algorithm and the factorization method in inverse scattering theory for inhomogeneous media, Inverse Probl. 18 (2002) 1025–1040.

[19] W.-K. Park, Interpretation of MUSIC for location detecting of small inhomogeneities surrounded by random scatterers, Math. Probl. Eng. 2016 (2016) 7872548.
[20] R. Song, R. Chen, X. Chen, Imaging three-dimensional anisotropic scatterers in multi-layered medium by MUSIC method with enhanced resolution, J. Opt. Soc. Am. A 29 (2012) 1900–1905.
[21] H. Ammari, E. Iakovleva, D. Lesselier, A MUSIC algorithm for locating small inclusions buried in a half-space from the scattering amplitude at a fixed frequency, Multiscale Model. Simul. 3 (2005) 597–628.
[22] R. Griesmaier, Reciprocity gap MUSIC imaging for an inverse scattering problem in two-layered media, Inverse Probl. Imaging 3 (2009) 389–403.
[23] E. Iakovleva, S. Gdoura, D. Lesselier, G. Perrusson, Multi-static response matrix of a 3D inclusion in half space and MUSIC imaging, IEEE Trans. Antennas Propag. 55 (2007) 2598–2609.
[24] H. Ammari, H. Kang, E. Kim, K. Louati, M. Vogelius, A MUSIC-type algorithm for detecting internal corrosion from electrostatic boundary measurements, Numer. Math. 108 (2008) 501–528.
[25] T. Henriksson, M. Lambert, D. Lesselier, Non-iterative MUSIC-type algorithm for eddy-current nondestructive evaluation of metal plates, in: Electromagnetic Nondestructive Evaluation (XIV), in: Stud. Appl. Electromagn. Mech., vol. 35, 2011, pp. 22–29.
[26] H. Ammari, H. Kang, H. Lee, W.-K. Park, Asymptotic imaging of perfectly conducting cracks, SIAM J. Sci. Comput. 32 (2010) 894–922.
[27] W.-K. Park, Asymptotic properties of MUSIC-type imaging in two-dimensional inverse scattering from thin electromagnetic inclusions, SIAM J. Appl. Math. 75 (2015) 209–228.
[28] W.-K. Park, D. Lesselier, Electromagnetic MUSIC-type imaging of perfectly conducting, arc-like cracks at single frequency, J. Comput. Phys. 228 (2009) 8093–8111.
[29] W.-K. Park, D. Lesselier, MUSIC-type imaging of a thin penetrable inclusion from its far-field multi-static response matrix, Inverse Probl. 25 (2009) 075002.
[30] S. Hou, K. Sølna, H. Zhao, A direct imaging algorithm for extended targets, Inverse Probl. 22 (2006) 1151–1178.
[31] S. Hou, K. Sølna, H. Zhao, A direct imaging method using far-field data, Inverse Probl. 23 (2007) 1533–1546.
[32] C.Y. Ahn, K. Jeon, W.-K. Park, Analysis of MUSIC-type imaging functional for single, thin electromagnetic inhomogeneity in limited-view inverse scattering problem, J. Comput. Phys. 291 (2015) 198–217.
[33] Y.-D. Joh, Y.M. Kwon, W.-K. Park, MUSIC-type imaging of perfectly conducting cracks in limited-view inverse scattering problems, Appl. Math. Comput. 240 (2014) 273–280.
[34] B. Scholz, Towards virtual electrical breast biopsy: space frequency MUSIC for trans-admittance data, IEEE Trans. Med. Imaging 21 (2002) 588–595.
[35] M. Cheney, The linear sampling method and the MUSIC algorithm, Inverse Probl. 17 (2001) 591–595.
[36] A. Kirsch, Characterization of the shape of the scatting obstacle using the spectral data of the far field operator, Inverse Probl. 14 (1998) 1489–1512.
[37] R. Kress, Inverse scattering from an open arc, Math. Methods Appl. Sci. 18 (1995) 267–293.
[38] L. Crocco, L.D. Donato, I. Catapano, T. Isernia, An improved simple method for imaging the shape of complex targets, IEEE Trans. Antennas Propag. 61 (2013) 843–851.
[39] J.C. Mosher, R.M. Leahy, Source localization using Recursively Applied and Projected (RAP) MUSIC, IEEE Trans. Signal Process. 47 (1999) 332–340.
[40] K. Agarwal, X. Chen, Y. Zhong, A multipole-expansion based linear sampling method for solving inverse scattering problems, Opt. Express 18 (2010) 6366–6381.
[41] A. Carpio, M.-L. Rapun, Solving inhomogeneous inverse problems by topological derivative methods, Inverse Probl. 24 (2008) 045014.
[42] G.R. Feijoo, A new method in inverse scattering based on the topological derivative, Inverse Probl. 20 (2004) 1819–1840.
[43] A. Litman, D. Lesselier, F. Santosa, Reconstruction of a 2-D binary obstacle by controlled evolution of a level-set, Inverse Probl. 14 (1998) 685–706.
[44] W.-K. Park, D. Lesselier, Reconstruction of thin electromagnetic inclusions by a level set method, Inverse Probl. 25 (2009) 085010.